Research Article Vol. 28, No. 6 / 16 March 2020 / Optics Express 8753
Optics EXPRESS

Linewidth reduction effect of a cavity-coupled dual-passband plasmonic filter

JINBO GAO,[1,2] JINSONG GAO,[1,2] ZIZHENG LI,[1,5] HAIGUI YANG,[1,4] HAI LIU,[1] XIAOYI WANG,[1] TONGTONG WANG,[1] KE WANG,[1,2] QIANG LI,[1] XIAOYI LIU,[3] YANCHAO WANG,[1] RUOQIAN GAO,[1,2] AND YUANHANG ZHAO[1,2]

[1]*Key Laboratory of Optical System Advanced Manufacturing Technology, Changchun Institute of Optics, Fine Mechanics and Physics, Chinese Academy of Sciences, Changchun 130033, China*
[2]*University of the Chinese Academy of Sciences, Beijing 100039, China*
[3]*Université Paris-Est, ESYCOM Lab., ESIEE Paris, Noisy-le-Grand 93162, France*
[4]*yanghg@ciomp.ac.cn*
[5]*lizizheng@ciomp.ac.cn*

Abstract: We propose a novel cavity-coupled MIM nano-hole array structure that exhibits a tunable dual passband in the near-infrared regime. When compared with the traditional single metal film, the designed structure provides a coupling effect between Gspp and SPP to significantly reduce the linewidths of the two transmission peaks. We also reveal the physical origin of the positive and negative influence of the cavity effect on the transmission of high-frequency and low-frequency peaks. This work supplies a new modulation theory for plasmonic devices based on the EOT phenomenon and has a wide application prospect in the fields of infrared sensor, plasmonic filter, and hyperspectral imaging.

1. Introduction

Plasmonics mainly concerns the interaction of light and matter limited to the wavelength or subwavelength scale [1–5]. When the incident electromagnetic wave operates in plasmonic nanostructures, the surface plasmons (SPs) can be excited due to the coherent oscillations of the free electrons in the metal. These surface plasmons fall into two categories: surface plasmon polaritons (SPPs) propagating at the metal-dielectric interface, and localized surface plasmons (LSPs) confined around the geometry of nanostructures [6–8]. The optical properties of the plasmonic metasurfaces such as amplitude [9], polarization [10], and phase [10,11] can be modulated by engineering the shape, size, and material of the nanostructures. Today, these structures attract a great deal of attention due to their thinness, which is much smaller than the operating wavelength. This characteristic makes the plasmonic optical components and systems easier to miniaturize and integrate. The devices prepared by the SPs principle have broad application prospects: biochemical sensors [12,13], waveguides [14], photocatalysts [15], surface-enhanced Raman scattering (SERS) [16,17], nanolasers [18], and energy harvester [19,20].

The extraordinary optical transmission (EOT) through subwavelength hole arrays was first reported by Ebbesen et al. in 1998 [21]. This transmission phenomenon produced by the resonant coupling between the SPPs on the corrugated metal surface and the incident light was far stronger than the prediction from classic Bethe theory. The filters prepared using this concept have the attractive characteristics of easy integration, miniaturization, and tunability. Some valuable related studies have been proposed [22–25]. More recently, related studies have attempted to adapt the complex aperture shapes, combination array, and hole-filling materials to improve the coupling efficiency between different SPP and LSP resonances and thereby affect the

#388544 https://doi.org/10.1364/OE.388544
Journal © 2020 Received 20 Jan 2020; revised 19 Feb 2020; accepted 24 Feb 2020; published 11 Mar 2020

Optics EXPRESS

spectral response of the passband [7,22,26]. However, a high-performance plasmonic filter with a narrower bandpass based on SPPs is still a great challenge. Furthermore, a more general theory including a simplified design can significantly modulate and improve the optical performance of the structure. In addition, related research usually focuses on experimental optical characteristics. Further investigations of the physical mechanism are also necessary.

In this paper, we have studied the optical properties of metal–insulator–metal (MIM) structures with periodic nano-hole arrays in the near-infrared (0.7–1.5 μm) region. We focus on the effect of a novel coupling mode for transmission. When compared with the traditional single metal film, the cavity effect brought by the MIM structure significantly reduces the full width at the half-maximum (FWHM) $\Delta\lambda$ of the dual transmission passband and improves the quality factor Q (Q=$\lambda_c/\Delta\lambda$, where λ_c is the center wavelength of the passband). It also greatly improves the transmittance of high-frequency resonance peak. This work provides a new modulation idea for similar plasmonic devices based on the principle of the EOT phenomenon. The characteristics of precise modulation and thinness make our MIM composite filters ideal for integration with appropriate photodetectors. There is high application value in fields such as infrared sensors, plasmonic filters, and hyperspectral imaging.

2. Simulation model

The optical characteristics of the cavity-coupled nano-hole system were theoretically analyzed by the 3D finite difference-time domain (FDTD) method using commercial software (Lumerical FDTD Solutions). The proposed structural model is shown in Fig. 1: the two gold films sandwich a SiO_2 layer of specific thickness H, and all MIM layers patterned with hexagonal-array "etch" holes are deposited on a quartz substrate. The upper surface of the substrate was set to the X-Y plane with Z = 0. In the simulation process, the normal X-polarized incident light with a wavelength range from 700 nm to 1500 nm propagates along the negative Z-direction. The asymmetric and symmetric boundary conditions align with the X- and Y-axes, respectively. They form the unit-cell "region" shown as the red dotted rectangle in Fig. 1. The condition of the perfectly matched layers (PML) swaps on the Z-boundaries. The permittivity of the Au and SiO_2 is extracted from the CRC and Palik model [27], respectively. The dielectric space is separated by the two metal layers in the Z direction. Therefore, both the metal films need to have a reasonable thickness to prevent the interfacial excitation SPP and the gap-cavity SPP from interfering with each other across the metal barrier. Based on the relevant concept of the penetration depth [9],

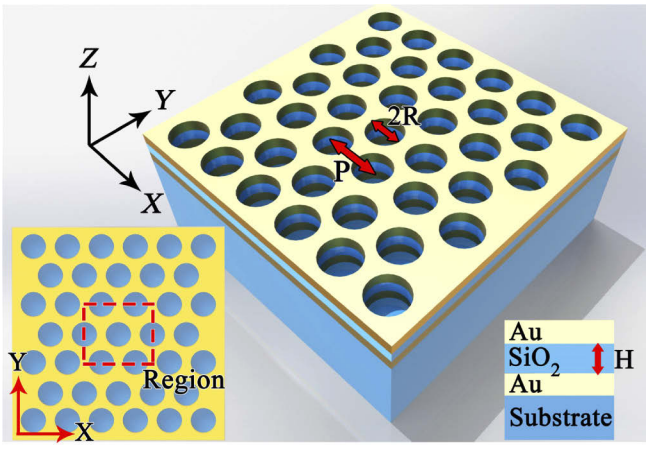

Fig. 1. Diagram of the designed cavity-coupled MIM nano-hole array structure. Top view and cross-sectional view of the structure.

Optics EXPRESS

we calculated that the sum maximum of penetration depth between the interfacial (including Air/Au and SiO_2/Au) SPP and the gap-cavity SPP in the gold layer is around 50 nm in the target passband. For the above considerations, we set this value to the thickness of the metal films. To ensure the correctness of the calculation results, the area containing the triple-layer MIM structure uses a discrete mesh grid with a size of 2 nm×2 nm×2 nm, and we performed multiple repeated verifications.

3. Theory analysis and numerical investigation

To better study the effect of cavity coupling on the plasmonic EOT phenomenon, we investigated the optical properties of a non-cavity 50-nm-thick gold layer deposited on the quartz substrate with a hexagonal nano-hole array as shown in Fig. 2(a). In the simulation calculation, we used the radius R as an independent variable and found that the structural transmission spectrum is a function of R and the incident wavelength with a fixed period P=800 nm and x-polarized E_{in} as shown in Fig. 2(b). Interestingly, the intensity and linewidths that are equivalent to FWHM of the two apparent transmission responses marked as T_1 at high frequencies and T_2 at low frequencies are affected by the changes in hole duty cycle; however, the peak resonant positions remain nearly constant located at specific wavelengths of 796 nm and 1129 nm. This is because the EOT phenomenon that originates from the SPPs excited at the metal-insulator (MI) interface effectively couples with the incident energy, and the excitation frequency of transmission-type SPPs is modulated by the structural period, arrangement type, and material characteristics independent of aperture radius. This property is attributed to the match between the surface plasmon dispersion and the grating coupling momentum in the wavenumber space. We defined the peak resonance positions of T_1 and T_2 as points 1 and 2 where P = 800 nm and R = 160 nm to facilitate subsequent analysis. In order to illustrate the role of SPPs in the EOT formation process, we can express the above relations by Eqs. (1) and (2) [9,22]:

$$k_{sp} = k_0 \sqrt{\frac{\varepsilon_m \varepsilon_d}{\varepsilon_m + \varepsilon_d}} \tag{1}$$

$$k_{\text{mode}} = k_0 \sin\theta + \sqrt{\frac{4}{3}(i^2 + i \cdot j + j^2)} \cdot G \tag{2}$$

Equation (1) indicates the wave vector threshold of the SPs excited on the MI interface, in which k_0=w/c is the wavenumber of the free-space incident light, and ε_m and ε_d are the permittivities of the metal and insulator medium, respectively. The source of the dielectric parameter model is described in the previous section. Equation (2) describes the Bragg coupling condition of the hexagonal array, where θ is the incidence angle, (i, j) represent the diffraction grating orders, and G signifies the reciprocal lattice vector, which is equal to 2π/P. Only when $k_{sp} = k_{mode}$, the incident light field is coupled to the SPs, and then the electromagnetic energy is trapped on the MI interface, increasing the transmission peak [28,29].

Figure 2(c) illustrates the dispersion relationships of SPs and different-order Bragg coupling obtained by solving Eqs. (1) and (2). In fact, it is possible for the MI interfaces on either side of the array of holes to sustain the SPs modes, which are offset from each other by the difference in ε_d of the asymmetric dielectric material directly contacting the metal layer. Therefore, the two sets of peaks revealed by the transmission spectrum correspond to different surface excitation modes [29]. The red and blue solid lines in Fig. 2(c) are the SPPs modes propagating at the external Air-Au interface and the internal SiO_2-Au interface, respectively. The red and blue dashed lines refer to the dispersion curves of light in vacuum and SiO_2 material. The discrete wavenumber increments of Bragg coupling with different resonance orders are represented by the green lines. Different diffraction wave vectors of $k_{mode}(1,0) = 9.069\times10^6$ m^{-1} and $k_{mode}(1,1) = 1.571\times10^7$ m^{-1} are derived from Eq. (2) with P=800 nm and θ=0. The intersection points I_1 and I_2 satisfying the

Optics EXPRESS

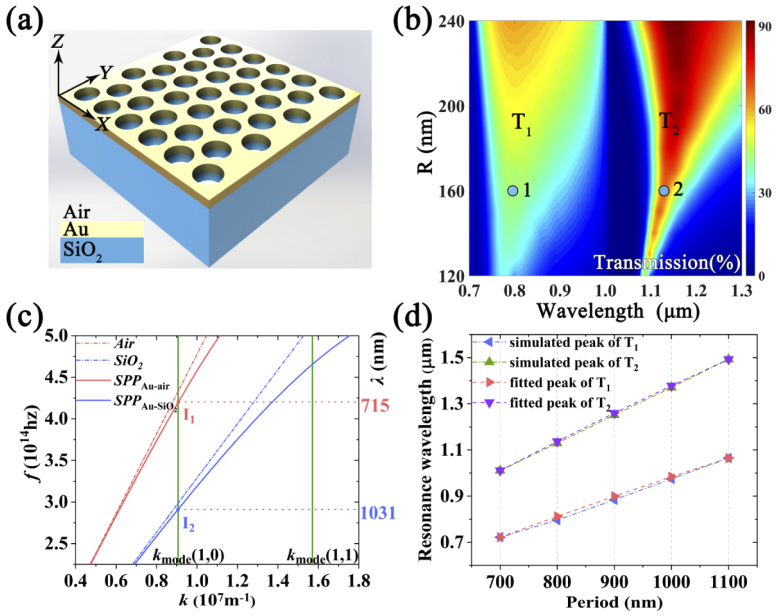

Fig. 2. (a) Diagram of the 50-nm-thick gold layer with hexagonal nano-hole array coated on the quartz substrate. Cross-sectional view of the structure. (b) Simulated transmission behavior for the gold single layer with the nano-hole array as a function of wavelength and the radius R of the hole with fixed period P = 800 nm. The points 1 and 2 indicate the transmission peaks of T_1 and T_2 with P = 800 nm and R = 160 nm, respectively. (c) The dispersion relation of SPs and different Bragg coupling orders. The wavenumber positions of the cross points I_1 and I_2 satisfy the wave-vector matching condition to excite the corresponding SPP mode. (d) The relationship between the P and transmission peak wavelengths of T_1 and T_2 obtained by FDTD and fitting method with the ratio of R/P = 0.2, respectively.

wave-vector matching condition $k_{sp} = k_{mode}$ exhibit excitation frequencies f_{I1}=4.196×10^{14} Hz and f_{I2}=2.910×10^{14} Hz that generate SPPs on Air-Au and SiO_2-Au surfaces, respectively. Therefore, the EOT peak wavelengths of the T_1 and T_2 modes are $\lambda_1(1,0) = 715$ nm and $\lambda_2(1,0) = 1031$ nm, corresponding to the previous simulation values of 796 nm and 1129 nm. Obviously, the peak wavelengths predicted by Eq. (2) appear at shorter wavelength positions, which is the result of neglecting the resonance phase shift caused by the in-hole coupling effects and the associated scattering losses [29]. To effectively predict the resonance peak position λ_r of each transmission mode, we propose the concept of effective refractive index $N_{eff} = k_{sp}/k_0$ and add a phase correction $\Delta\varphi$ to the constructed mathematical model, which is expressed as Eq. (3):

$$\lambda_r = \frac{N_{eff} \cdot P}{\sqrt{\frac{4}{3}(i^2 + i \cdot j + j^2)} + \frac{\Delta\varphi}{2\pi}} \tag{3}$$

Naturally, since the diffraction order can be obtained from the dispersion relation, as long as we know the trend of N_{eff} and $\Delta\varphi$, we can quickly solve for λ_r. Taking as an example, the two transmission relationships of T_1 extracted by periodic scanning with the condition of R/P = 0.2 shown in Fig. 2(d), we get the exact values of N_{eff} and $\Delta\varphi/2\pi$ when P=700 nm (1.031 and -0.155) and P=1100 nm (1.011 and -0.111) from Eqs. (1)–(3). Hence, the phase shift $\Delta\varphi$ and the effective refractive index N_{eff} of other periods in the T_1 mode can be obtained by linear fitting, and then all the resonant wavelengths λ_rs in the desired working band will be calculated. Of

Optics EXPRESS

course, the same calculation method can be applied to the T_2 mode. The relationships between the simulated peak positions and the corresponding λ_rs acquired by fitting are also illustrated in Fig. 2(d). It is clear that the results of T_1 and T_2 modes calculated by the two methods are in good agreement. The positive correlation between P and λ_r represented by Eq. (3) can explain the linear redshift phenomenon of the resonant wavelengths with periodic modulation. Therefore, within a reasonable range, this fitting theory is a fast and convenient way to obtain the peak solution of the relevant model, avoiding large amounts of repeated simulations.

The near-field distributions around holes excited at the two transmission peaks of T_1 and T_2 are necessary to further illustrate the nature of the resonant hole excitations. As shown in Figs. 3(a) and 3(b), when P = 800 nm and R = 160 nm, the relative magnetic field energy $|H/H_0|^2$ on the X-Z plane is mainly confined to the Air-Au and SiO_2-Au interfaces, and the corresponding decay length is significantly shorter in the metal than in the dielectric. This indicates that the SPP modes are excited by the coupling of the incident energy with the periodic nanohole array. Furthermore, the maximum electric field enhancement is observed near the hole edges as shown in Figs. 3(c) and 3(d), because the charge accumulation associated with dipolar excitation is the largest at these locations [30,31]. Of course, the relative electric field distributions $|E/E_0|$ of LSPs in the two modes behave differently. The strongest field enhancement is localized around the top of the opening of the hole at the wavelength of feature point 1 but occurs near the bottom of the hole at point 2. This difference also corresponds to the generation surface of the particular SPP mode. The LSP phenomenon at the edges of the holes acts as an effective dipole scatterer, which can re-excite surface waves along the hole wall in the Z-direction, thereby enhancing the coupling between the holes and SPP. This view is confirmed by the Ez-field distribution of Figs. 3(e) and 3(f) in the hole located at the middle of the thickness of the metal layer (Z=25 nm) on the X-Y plane. There is a clear surface wave flowing toward the inner side wall of the hole, with a dipole-like radiation pattern. Therefore, we speculate that the essence of the EOT phenomenon is the joint coupling of the SPP formed at the interface and the side-wall modes excited by LSP.

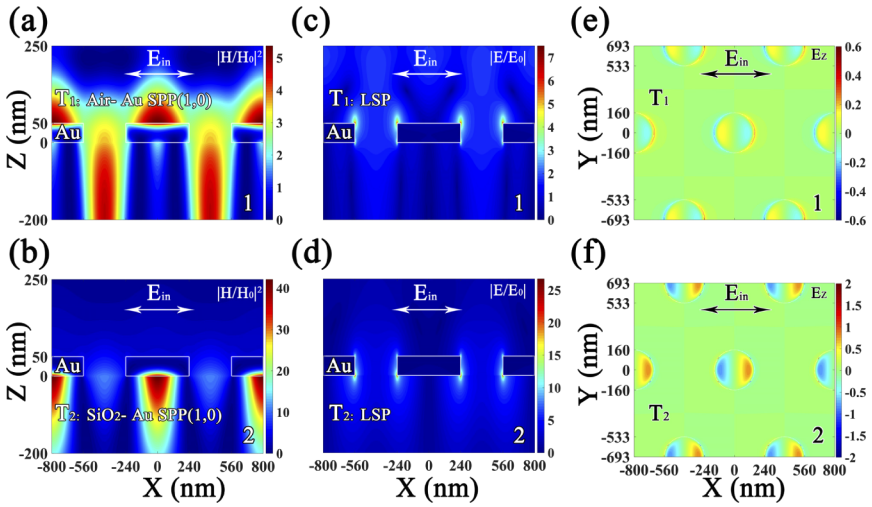

Fig. 3. (a) and (b) Longitudinal relative magnetic-field energy distributions at the wavelengths of T_1's and T_2's transmission peaks when R is 160 nm and P is 800 nm. The color bars stand for the normalized magnetic energy intensity. (c) and (d) Longitudinal relative electric-field intensity distributions at points 1 and 2, respectively. The color bars stand for the normalized electric field intensity. (e) and (f) The relative electric field E_z distributions at points 1 and 2, respectively, on the X–Y plane with Z=25 nm. The color bars stand for the normalized electric field E_z intensity.

Optics EXPRESS

In the previous section, we discussed the EOT phenomenon of a gold film with hexagonal nano-hole array, and we noticed that its characteristic spectrum shows poor transmittance and wide FWHM value in T_1 mode. In order to improve the spectral performance, we have improved the single-layer metal design to a MIM resonance structure coated on the quartz substrate, which consists of 50 nm thickness on both the top and bottom Au layer, and an initial value of H=50 nm thickness for the middle SiO_2 gap with patterned nano-hole array as shown in Fig. 1. For the purpose of comparison with the previous study, we scanned the radius R of the nanoholes at fixed P=800 nm and obtained the transmission performance under the influence of R and incident wavelength for the composite structure shown in Fig. 4(a). The evident difference from Fig. 2(b) is that a transmission valley marked as A_1 appears, which causes the T_1 mode to split and significantly reduces the linewidth of the main peak and increases its transmittance. The A_1 resonance state is actually caused by the Gap SPP (Gspp), which will be discussed later. It is not difficult to understand that the shift of T_1 and T_2 resonance peak positions is attributed to the phase shift caused by the coupling of Gspp with the original SPP modes. To reflect these characteristics directly, we compared the spectral behaviors between the single-layer metal and the MIM structure with hole radius of R=160 nm at a fixed period (P = 800 nm) as shown in Fig. 4(b). The spectral transmission linewidth (74 nm) of the MIM structure in the T_1 mode reduces by 2/3 compared to the single-layer metal (228.7 nm), and the quality factor Q increases from 3.48 to 10.53. At the same time, the transmittance of the main peak increased by 23.6%. The absorption curve of the MIM structure with R=160 nm and P = 800 nm as shown in Fig. 4(b) reveals that the nature of the A_1 mode is a strong energy localization and absorption caused by the gap's cavity effect. In addition, the excitation process of SPP requires the participation of metallic materials, so that the T_1 and T_2 transmission modes inevitably produce some by-products of absorption loss. It is foreseeable that as the hole radius R continues to increase, more and more light fields are coupled into the hole, and the transmittance of the side peak becomes stronger and cannot be ignored, leading to significant crosstalk. Therefore, the ratio R/P is adopted as 0.2, which is a trade-off between linewidth optimization and side peak suppression.

In fact, the Gspp excited on the two SiO_2-Au interfaces forms a standing wave along the SiO_2 gap of the MIM structure between the SiO_2-Air boundaries in A_1 mode, and the electric energy has a transverse nodal arrangement consisting of alternating bright and dark regions as shown in Fig. 4(c). Hence, the MIM structure is equivalent to the role of a transverse Fabry-Perot (F-P) cavity [32–34], providing a unique modulation method. The excitation state of Gspp can be described using the waveguide model and dispersion relationship given by Eqs. (4) and (5) [35–38]:

$$2\beta L + \Delta\varphi' = 2\sqrt{m^2 + n^2}\pi \tag{4}$$

$$\varepsilon_d k_m + \varepsilon_m k_d \tanh(\frac{k_d}{2}\mathrm{H}) = 0 \tag{5}$$

where β is the wave vector of the Gspp, L = P-2R is the transverse length of the F-P cavity, $\Delta\varphi'$ is the round-trip phase shift of the reflection at the two end-face boundaries, and m and n are the resonant orders, which denote the number of intensity antinodes (or nodes) in the X- and Y-directions, respectively. The parameters k_d and k_m are defined as $k_d = (\beta^2 - \varepsilon_d k_0^2)^{1/2}$ and $k_m = (\beta^2 - \varepsilon_m k_0^2)^{1/2}$. In the A_1 resonance state at point 3, both the SPP induced by the top and bottom interfaces of the MIM structure and the radiation pattern in the hole have all disappeared. At this time, the energy carrier is Gspp, which is localized in the F-P cavity as shown in Fig. 4(c). The relative electric field distributions and Poynting vectors in Fig. 4(d) are calculated in the center thickness X-Y plane (Z=75 nm) of the dielectric gap, which directly reflects the Gspp field resonance order as (2,2) and immediately describes the energy flowing from the hole to the F-P cavity as forming an internal circulation. By combining the Eqs. (4) and (5), we calculated the effective refractive index N_{eff}'=2.14 (N_{eff}' is defined as β/k_0) and the additional phase shift $\Delta\varphi'/2\pi$=0.41 in the MIM cavity at point 3. Based on the above theory, we can clearly explain the

Optics EXPRESS

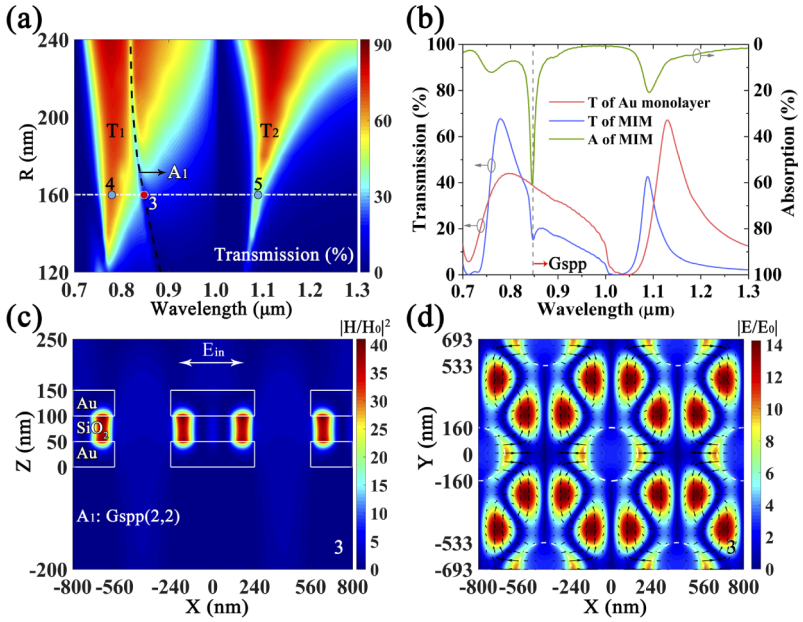

Fig. 4. (a) Simulated transmission behavior for the MIM structure with the nano-hole array as a function of wavelength and the radius R of the hole with fixed period P = 800 nm. The black and white dashed curves indicate the locations of A_1 resonance and transmission with R=160 nm, respectively. The cross points 3 to 5 reflect the three transmission extreme values of A_1, T_1, and T_2. (b) Under the condition of R=160 nm and P=800 nm, the transmission spectra of the single-layer metal and the MIM structure with nano-hole array show a clear difference, and the corresponding absorption curve of the MIM structure is also exhibited. (c) Longitudinal relative magnetic-field energy distribution at point 3. The color bar stands for the normalized magnetic energy intensity. (d) The relative electric-field intensity distributions on the X-Y plane with Z=75 nm at point 3. The color bar stands for the normalized electric field intensity, and the black arrows represent the Poynting vectors. The outline of the nanohole is marked by a white dotted line.

blue shift phenomenon of A_1 mode in the radius modulation process in Fig. 4(a): As the radius R of the nanohole gets larger, the resonance length L of the F-P cavity becomes shorter. The changes in $\Delta\varphi'$ are actually rather subtle in this process, and there is a tendency to maintain the resonance order (m=2, n=2) at the resonant wavelength of A_1 mode. Thus, we can predict that the resonant wavenumber (β) will increase due to the decrease of L, and the peak frequency of the Gspp mode will shift toward the short-wave direction.

We will clarify the specific influence of the MIM cavity effect on the two transmission modes. The significant reduction in the linewidth of T_1 is attributed to the strong absorption caused by the energy localization of Gspp (2,2) in A_1, which causes the spectral transmission to drop sharply and also significantly affects the quality factor. At the peak frequency of T_1 at point 4, the Gspp mode located in the gap cavity is in the transition process from the (2,2) to the (2,3) order. The unstable Gspp (2,3) basically shows a resonance integer order between adjacent holes and is coupled with Air-Au SPP (1,0). This coupling effect significantly enhances the radiant energy in the hole as shown in Fig. 5(a) and improves the spectral transmittance of the structure. Figure 5(c) shows the arrangement of the electric field response in the center plane of the gap thickness (Z=75 nm) and shows that the energy flows from the gap cavity through the end-face boundary into the hole, which also confirms the statement that Gspp can gain the T_1 transmission. At the T_2 peak frequency corresponding to point 5, SiO_2-Au SPP (1,0) is still the

Optics EXPRESS

origin of induced transmission as shown in Fig. 5(b), but this spectral position is far from the adjacent stable Gspp resonance frequency. In this case, the field distribution in the dielectric gap during the cavity-to-hole transition process will cause a forced resonance in the F-P cavity due to the mismatch of wave vectors. Naturally, the energy flowing into the cavity cannot be enhanced by resonance, but instead gradually disappears in the cavity due to the damping loss. Therefore, the gap cavity is equivalent to a loss device, which plays a negative role in T_2 mode. For this reason, the attenuation of the T_2 transmission is steeper, resulting in the linewidth decreasing from 79.3 to 38.7, and the Q value increasing from 14.2 to 28.1. Figure 5(d) shows the specific process of energy entering into the MIM cavity from the hole and eventually dissipating in the cavity, which is consistent with the above theory.

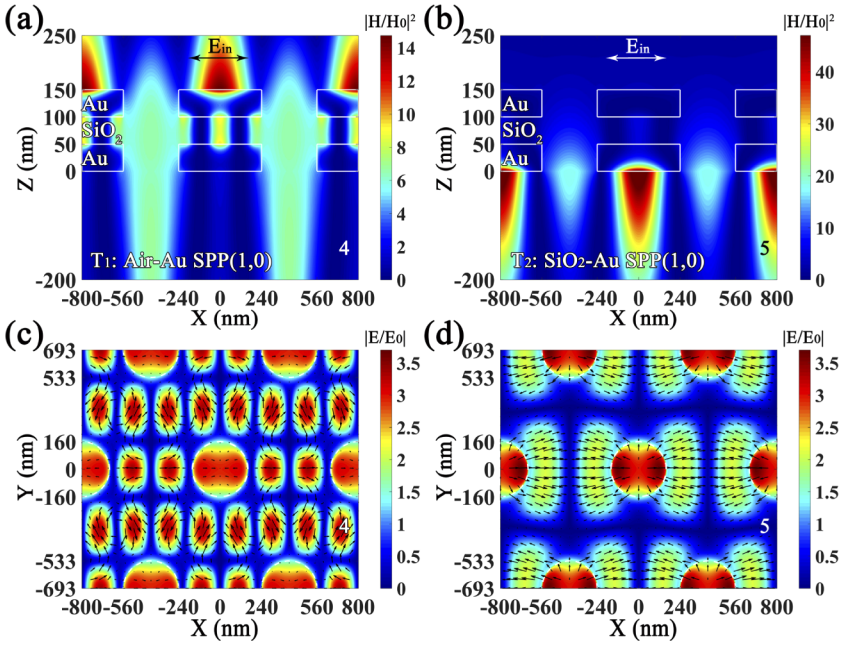

Fig. 5. (a) and (b) Longitudinal relative magnetic-field energy distributions at point 4 and point 5, respectively. The color bars stand for the normalized magnetic energy intensity. (c) and (d) The relative electric-field intensity distributions on the X-Y plane with Z=75 nm at point 4 and point 5, respectively. The color bar stands for the normalized electric field intensity, and the black arrows represent the Poynting vectors. The outline of the nanohole is marked by a white dotted line.

Finally, we discuss the optimization of the dielectric-cavity thickness H. From Eq. (5), we can infer that tuning the thickness of the dielectric gap can change the resonant wave vector β and reshape the spectral response. Furthermore, Fig. 6(a) depicts the different behaviors of five transmission plots with H increasing from 30 to 70 nm. When H< 50 nm, there are both Gspp (2,2) and Gspp (2,3) modes in the transmission spectra marked by red and black dotted arrows, respectively. As H increases, the corresponding characteristic solution β in the MIM cavity becomes larger, making the two transmission valleys continuously blue-shift. However, unless H = 50 nm, there will be multiple side peaks or excessive noise in the T_1 band. When H> 50 nm, the A_1 absorption gradually works around the T_1 peak. Unfortunately, the Gspp (2,2) resonance mode at this time cannot perfectly cancel out the transmission excited by Air-Au SPP (1,0), resulting in the high intensity of the side peak. A similar phenomenon will occur when the duty cycle R/P is too large. Figure 6(b) shows the stable Gspp (2,2) and Gspp (2,3) modes'

Optics EXPRESS

electric field and energy flow distributions at the center thickness of the gap where P = 800 nm, R = 160 nm, and H = 40 nm. It is worth noting that in the absorption mode with stable Gspp, there is almost no radiation pattern in the hole, which is the exact opposite of the transmission mode. The physical mechanism of the former two modes is similar to the A_1 mode at point 3 and is not repeated here. Additionally, when the structural period is tuned with a constant ratio of R/P=0.2, the peak wavelengths of corresponding spectral curves, which display stable and similar waveforms, can be modulated as shown in Fig. 6(c). This result suggests that the two transmission peaks that maintain narrow linewidths can be controlled simultaneously by shifting the period into two focused infrared operating bands, thereby generating a dual infrared response band device. The extreme wavelengths of T_1, A_1, and T_2 with different periods can also be quickly solved by the linear fitting method mentioned above. However, the calculation formula of the A_1's resonance wavelength is converted to $\lambda_G = 2N_{eff}' \cdot L/(\sqrt{m^2+n^2} - \Delta\varphi'/2\pi)$. The parameter pair ($N_{eff}'$, $\Delta\varphi'/2\pi$) of the gap cavity in Gspp (2,2) mode is obtained with Eqs. (4) and (5) as (2.185, 0.420) with P=700 nm and (2.072, 0.391) with P=1100 nm. The simulated and fitted results shown in Fig. 6(d) are in good agreement.

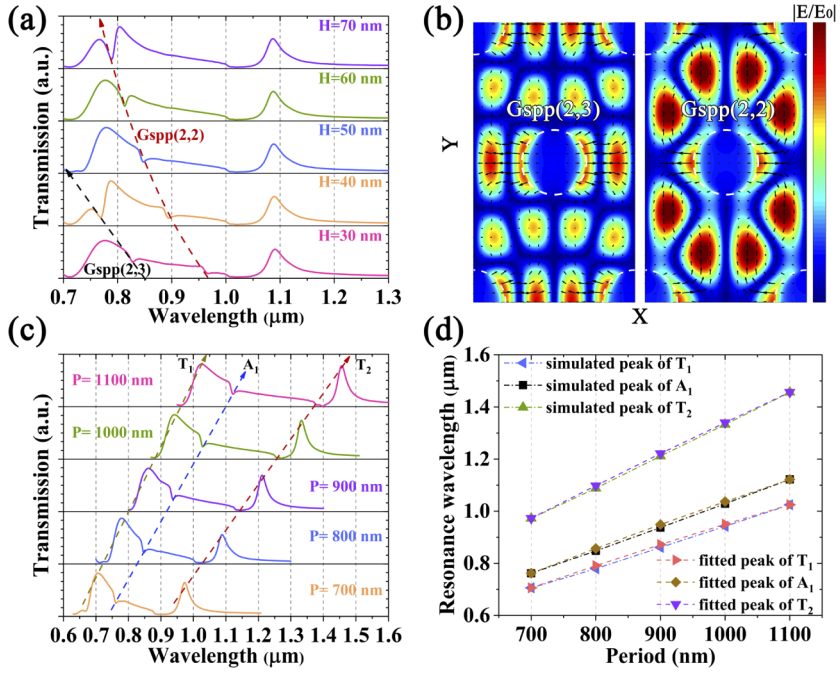

Fig. 6. (a) The transmission behaviors of the proposed structure with H increasing from 30 to 70 nm at fixed P = 800 nm and R/P=0.2. The red and black dotted arrows indicate the resonance positions of Gspp(2,2) and Gspp(2,3). (b) The relative electric-field intensity distributions of Gspp(2,3) and Gspp(2,2) at the center thickness of the gap with H=40 nm. The color bar stands for the normalized electric field intensity, and its upper limit is $|E/E_0|$=12. The black arrows represent the Poynting vectors. (c) The dependence of transmission on the P of the proposed structure in the passband with fixed H=50 nm and the ratio of R/P=0.2. (d) The relationship between the P and extreme wavelength of T_1, A_1, and T_2 obtained by FDTD and fitting method with the ratio of R/P = 0.2, respectively.

Optics EXPRESS

4. Conclusion

In summary, we have investigated a promising plasmonic filter of MIM structure with a nano-hole array in the working region of 0.7–1.5 μm, which provides a coupling effect between the SPP mode on the MI interface and Gspp in the gap cavity. Based on the cavity effect, the optical characteristics of dual passbands show significant improvement in linewidth and quality factor compared to the single metal film. The influence of the transverse F-P cavity on the transmittance was also discussed, which includes the energy gain to the high-frequency T_1 peak and the induced additional losses for the low-frequency T_2 peak. In addition, we provided optimized results for the nano-hole radius R and the gap-layer thickness H to further promote the noise suppression at high-frequency transmission. The advantages of periodic modulation, miniaturization, and simple hole shape are suitable for integration with photodetectors.

Funding

National Natural Science Foundation of China (11604329, 61675199, 61705226, 61875193, 61905238); Changchun Science and Technology Bureau (19SS004); Department of Science and Technology of Jilin Province (20190201126JC, 20190302082GX).

Disclosures

The authors declare no conflicts of interest.

References

1. T. Allsop, R. Arif, R. Neal, K. Kalli, V. Kundrat, A. Rozhin, P. Culverhouse, and D. J. Webb, "Photonic gas sensors exploiting directly the optical properties of hybrid carbon nanotube localized surface plasmon structures," Light: Sci. Appl. **5**(2), e16036 (2016).
2. C. F. Guo, T. Sun, F. Cao, Q. Liu, and Z. Ren, "Metallic nanostructures for light trapping in energy-harvesting devices," Light: Sci. Appl. **3**(4), e161 (2014).
3. M. L. Brongersma, "Introductory lecture: nanoplasmonics," Faraday Discuss. **178**, 9–36 (2015).
4. F. Pincella, K. Isozaki, and K. Miki, "A visible light-driven plasmonic photocatalyst," Light: Sci. Appl. **3**(1), e133 (2014).
5. X. Liu, J. Gao, J. Gao, H. Yang, X. Wang, T. Wang, Z. Shen, Z. Liu, H. Liu, J. Zhang, Z. Li, Y. Wang, and Q. Li, "Microcavity electrodynamics of hybrid surface plasmon polariton modes in high-quality multilayer trench gratings," Light: Sci. Appl. **7**(1), 14 (2018).
6. Y. Chu, M. G. Banaee, and K. B. Crozier, "Double-Resonance Plasmon Substrates for Surface-Enhanced Raman Scattering with Enhancement at Excitation and Stokes Frequencies," ACS Nano **4**(5), 2804–2810 (2010).
7. L. Lin and A. Roberts, "Light transmission through nanostructured metallic films: Coupling between surface waves and localized resonances," Opt. Express **19**(3), 2626–2633 (2011).
8. Y. Chu and K. B. Crozier, "Experimental study of the interaction between localized and propagating surface plasmons," Opt. Lett. **34**(3), 244–246 (2009).
9. W. L. Barnes, "Surface plasmon–polariton length scales: a route to sub-wavelength optics," J. Opt. A: Pure Appl. Opt. **8**(4), S87–S93 (2006).
10. Y. Zhao and A. Alù, "Manipulating light polarization with ultrathin plasmonic metasurfaces," Phys. Rev. B: Condens. Matter Mater. Phys. **84**(20), 205428 (2011).
11. T. Cao, S. Wang, and W. X. Jiang, "Tunable metamaterials using a topological insulator at near-infrared regim," RSC Adv. **3**(42), 19474–19480 (2013).
12. A. E. Cetin, D. Etezadi, B. C. Galarreta, M. P. Busson, Y. Eksioglu, and H. Altug, "Plasmonic Nanohole Arrays on Robust Hybrid Substrate for Highly Sensitive Label-Free Biosensing," ACS Photonics **2**(8), 1167–1174 (2015).
13. B. Park, S. H. Yun, C. Y. Cho, Y. C. Kim, J. C. Shin, H. G. Jeon, Y. H. Huh, I. Hwang, K. Y. Baik, Y. I. Lee, H. S. Uhm, G. S. Cho, and E. H. Choi, "Surface plasmon excitation in semitransparent inverted polymer photovoltaic devices and their applications as label-free optical sensors," Light: Sci. Appl. **3**(12), e222 (2014).
14. R. F. Oulton, V. J. Sorger, D. A. Genov, D. F. P. Pile, and X. Zhang, "A hybrid plasmonic waveguide for subwavelength confinement and long-range propagation," Nat. Photonics **2**(8), 496–500 (2008).
15. X.-C. Ma, Y. Dai, L. Yu, and B.-B. Huang, "Energy transfer in plasmonic photocatalytic composites," Light: Sci. Appl. **5**(2), e16017 (2016).
16. P. Zheng, M. Li, R. Jurevic, S. K. Cushing, Y. Liu, and N. Wu, "A gold nanohole array based surface-enhanced Raman scattering biosensor for detection of silver(i) and mercury(ii) in human saliva," Nanoscale **7**(25), 11005–11012 (2015).

Optics EXPRESS

17. P. Zheng, S. K. Cushing, S. Suri, and N. Wu, "Tailoring plasmonic properties of gold nanohole arrays for surface-enhanced Raman scattering," Phys. Chem. Chem. Phys. **17**(33), 21211–21219 (2015).
18. S. Wang, X.-Y. Wang, B. Li, H.-Z. Chen, Y.-L. Wang, L. Dai, R. F. Oulton, and R.-M. Ma, "Unusual scaling laws for plasmonic nanolasers beyond the diffraction limit," Nat. Commun. **8**(1), 1889 (2017).
19. J. Y. Lu, S. H. Nam, K. Wilke, A. Raza, Y. E. Lee, A. AlGhaferi, N. X. Fang, and T. Zhang, "Localized Surface Plasmon-Enhanced Ultrathin Film Broadband Nanoporous Absorbers," Adv. Opt. Mater. **4**(8), 1255–1264 (2016).
20. Y. Qu, Q. Li, H. Gong, K. Du, S. Bai, D. Zhao, H. Ye, and M. Qiu, "Spatially and Spectrally Resolved Narrowband Optical Absorber Based on 2D Grating Nanostructures on Metallic Films," Adv. Opt. Mater. **4**(3), 480–486 (2016).
21. T. W. Ebbesen, H. J. Lezec, H. F. Ghaemi, T. Thio, and P. A. Wolff, "Extraordinary optical transmission through sub-wavelength hole arrays," Nature **391**(6668), 667–669 (1998).
22. Q. Chen and D. R. S. Cumming, "High transmission and low color cross-talk plasmonic color filters using triangular-lattice hole arrays in aluminum films," Opt. Express **18**(13), 14056–14062 (2010).
23. Y. S. Do, J. H. Park, B. Y. Hwang, S.-M. Lee, B.-K. Ju, and K. C. Choi, "Plasmonic Color Filter and its Fabrication for Large-Area Applications," Adv. Opt. Mater. **1**(2), 133–138 (2013).
24. I. J. H. McCrindle, J. P. Grant, L. C. P. Gouveia, and D. R. S. Cumming, "Infrared plasmonic filters integrated with an optical and terahertz multi-spectral material," Phys. Status Solidi A **212**(8), 1625–1633 (2015).
25. S.-H. Hwang, M.-J. Kim, S. Jeon, B. Shin, and J.-H. Jeong, "Plasmonic color filters fabricated via oxide-based nanotransfer printing," Nanotechnology **29**(41), 415301 (2018).
26. Y.-W. Jiang, L. D.-C. Tzuang, Y.-H. Ye, Y.-T. Wu, M.-W. Tsai, C.-Y. Chen, and S.-C. Lee, "Effect of Wood's anomalies on the profile of extraordinary transmission spectra through metal periodic arrays of rectangular subwavelength holes with different aspect ratio," Opt. Express **17**(4), 2631–2637 (2009).
27. E. D. Palik, *Handbook of Optical Constants of Solids* (Academic, 1985).
28. W. L. Barnes, A. Dereux, and T. W. Ebbesen, "Surface plasmon subwavelength optics," Nature **424**(6950), 824–830 (2003).
29. C. Genet and T. W. Ebbesen, "Light in tiny holes," Nature **445**(7123), 39–46 (2007).
30. T. Rindzevicius, Y. Alaverdyan, B. Sepulveda, T. Pakizeh, M. Kall, R. Hillenbrand, J. Aizpurua, and F. J. G. d. Abajo, "Nanohole Plasmons in Optically Thin Gold Films," J. Phys. Chem. C **111**(3), 1207–1212 (2007).
31. G. Schaffernak, M. K. Krug, M. Belitsch, M. Gasparic, H. Ditlbacher, U. Hohenester, J. R. Krenn, and A. Hohenau, "Plasmonic Dispersion Relations and Intensity Enhancement of Metal-Insulator-Metal Nanodisks," ACS Photonics **5**(12), 4823–4827 (2018).
32. K. Tanaka and M. Tanaka, "Simulations of nanometric optical circuits based on surface plasmon polariton gap waveguide," Appl. Phys. Lett. **82**(8), 1158–1160 (2003).
33. J. Chen, P. Wang, Z. M. Zhang, Y. Lu, and H. Ming, "Coupling between gap plasmon polariton and magnetic polariton in a metallic-dielectric multilayer structure," Phys. Rev. E: Stat., Nonlinear, Soft Matter Phys. **84**(2), 026603 (2011).
34. J. Gao, J. Gao, H. Yang, H. Liu, X. Wang, K. Wang, X. Liu, Q. Li, Y. Wang, Z. Li, R. Gao, and Z. Zhang, "Cavity-driven hybrid plasmonic ultra-narrow bandpass filter," Opt. Express **27**(15), 20397 (2019).
35. X. L. Zhu, Y. Ma, J. S. Zhang, J. Xu, X. F. Wu, Y. Zhang, X. B. Han, Q. Fu, Z. M. Liao, L. Chen, and D. P. Yu, "Confined Three-Dimensional Plasmon Modes inside a Ring-Shaped Nanocavity on a Silver Film Imaged by Cathodoluminescence Microscopy," Phys. Rev. Lett. **105**(12), 127402 (2010).
36. S.-H. Chang and Y.-L. Su, "Mapping of transmission spectrum between plasmonic and nonplasmonic single slits. I: resonant transmission," J. Opt. Soc. Am. B **32**(1), 45–51 (2015).
37. F. F. Hu, H. X. Yi, and Z. P. Zhou, "Band-pass plasmonic slot filter with band selection and spectrally splitting capabilities," Opt. Express **19**(6), 4848–4855 (2011).
38. J. Petschulat, C. Helgert, M. Steinert, N. Bergner, C. Rockstuhl, F. Lederer, T. Pertsch, A. Tünnermann, and E. B. Kley, "Plasmonic modes of extreme subwavelength nanocavities," Opt. Lett. **35**(16), 2693–2695 (2010).